

# In-vitro Ant Biofilm Effect of Green-Approach Magnesium Oxide Nanoparticles Synthesised Using Non-thermal Plasma Technique

Abdulkader Makki Dahham,¹ Nisreen Kh. Abdalameer,²\* Fatima J. Hassan³ and Raghad S. Mohammed⁴

<sup>1</sup>Ibn Sina University of Medical and Pharmaceutical Sciences, Qadisaya Expy, Baghdad, Iraq <sup>2</sup>Department of Physics, College of Science for Women, Baghdad University, Baghdad, Iraq <sup>3</sup>Department of Medical Laboratory Techniques, College of Health and Medical Techniques, Al-Mustafa University, Baghdad, Iraq

<sup>4</sup>Department of Physics, College of Science, Mustansiriyah University, Baghdad, Iraq

\*Corresponding author email: nisreenka\_phys@csw.uobaghdad.edu.iq

Published online: 28 November 2025

**To cite this article:** Dahham, A. M. et al. (2025). In-vitro ant biofilm effect of green-approach magnesium oxide nanoparticles synthesised using non-thermal plasma technique. *J. Phys. Sci.*, 35(3), 27–42. https://doi.org/10.21315/jps2025.36.3.3

To link this article: https://doi.org/10.21315/jps2025.36.3.3

ABSTRACT: Microbial infectious illnesses pose a global health risk due to antibiotic misuse, leading to antimicrobial-resistant microorganisms. Nanotechnology offers potential solutions to combat these pathogens. Magnesium oxide nanoparticles (MgO NPs) have emerged as a promising option for combating antibiotic-resistant microorganisms. Their diverse physicochemical features allow them to function as antibacterial agents. This research focuses on synthesising MgO NPs using a green method, plasma-assisted reduction and an aqueous dill extract as a stabilising agent. This technology is environmentally favourable due to its safety, cost-effectiveness, rapid fabrication and lack of hazardous-reducing agents. The crystal size, particle size, morphology, elemental composition and optical characteristics of MgO NPs were determined using various methods. MgO NPs exhibited a dendritic morphology with diameters in the nanometre scale. The mean crystal size was determined to be 38.93 nm using X-ray diffraction (XRD) examination. ultraviolet-visible (UV-Vis) spectroscopy research demonstrated that the absorption of MgO NPs produces a peak at 295 nm, signifying an energy band gap of 4.2 eV. At a concentration of 10 mgL<sup>-1</sup>, the antibiofilm effectiveness of MgO NPs was evaluated against Staphylococcus aureus (S. aureus) (Gram-positive) and Klebsiella pneumonia (K. pneumonia), Escherichia coli (E. coli) (Gramnegative) bacteria. The biofilm inhibition rate of MgO NPs against S. aureus exceeded that against K. pneumoniae and E. coli. This study indicates that MgO NPs synthesised by a green technique had substantial antibiofilm activity and showed a remarkable potential for inhibiting pathogenic microorganisms.

Keywords: Cold plasma, MgO NPs, Antibiofilm, K. pneumonia, E. coli, S. aureus

#### 1. INTRODUCTION

Biofilms are colonies of microorganisms that consist of hundreds of different species interacting with one another and with the substrate or interface to which they are attached. In biofilms, cells are encased in an extracellular polymeric material matrix that the cells themselves manufacture. This matrix serves many purposes: first, as a physical barrier against outside invaders; second, it allows the cells in the community to work together efficiently; and third, it stores nutrients. Biofilms play a significant role in healthcare-associated illnesses, of which about half are linked to using an indwelling medical device.<sup>2</sup> They are thought to be responsible for about 80% of all chronic infections in humans.<sup>3</sup> Around 37,000 people died directly because of healthcareassociated diseases, which affected more than 4 million people in European hospitals in 2008. In the United States, the incidence of such diseases exceeded 1,7 million in 2002, resulting in over 100,000 related fatalities. Illnesses associated with medical equipment were the first clinical diseases recognised as having a biofilm aetiology.<sup>4,5</sup> Millions of medical devices are used annually, so biofilms pose a considerable public health threat to individuals dependent on these devices. <sup>4,6</sup> Compared to their planktonic counterparts, bacterial cells in biofilms exhibit a remarkable resistance to antibiotics and antimicrobial agents. Since the extracellular polymeric substances (EPS) matrix acts as an insulator, it restricts the ability of antimicrobial drugs to penetrate the biofilm, which is thought to be the primary cause of the antimicrobial tolerance.<sup>7</sup> As a result, substantial concentrations of antimicrobial drugs are required to destabilise biofilms and cure biofilm-associated infections. The dramatic rise in diseases caused by antibiotic-resistant bacteria and the problems in treating them has motivated the adoption of nanomaterials.8 Magnesium oxide (MgO) as a nanoparticles (NPs) has grown in popularity, particularly in the field of medicine, where it is used for diagnostics, detection and molecular behaviour biosensors. 9 The antibacterial impact of NPs based on MgO has shown effective effects on a broad variety of microorganisms, for whom the antibacterial mechanism of action is related to the size and dose dependency. 10,111 Physical and chemical procedures have been used to create NPs from various materials. NPs may be created using a variety of processes, including pulsed laser deposition, solegel preparation, chemical coprecipitation, thermal breakdown and hydrothermal procedures. Plasma jets and microwaves have recently received a lot of interest as leading "green technologies" for nanomaterial production. Plasma jet technique provides various benefits and advantages, including environmental friendliness, cheap cost and no need for costly equipment. 12 Bio-reduction transpires in three separate steps. In the activation phase, metal ions are reduced, and nucleation occurs due to enzymes secreted by algal cells, shown by a colour change in the solution. During the growth phase, the nucleated metallic elements amalgamate, yielding thermodynamically stable NPs of various sizes and forms. <sup>13</sup> Nanomaterial production via plasma-liquid interactions is a relatively recent topic of plasma research that is quickly expanding. This is a consequence of many newly identified plasma generators operating at low to atmospheric pressures. 14,15 Many plant materials are accessible

for green NP synthesis, and various researchers have explored local, plentiful species. This research allows local plants to be used, but worldwide manufacturing of greensynthesised nanoscale metals is problematic. Over the last two decades, the synthesis of metallic and non-metallic NPs has led to the development of several manufacturing processes, resulting in diverse sizes, shapes and compositions of NPs. Historically, the techniques for synthesising and stabilising NPs have relied on physical and chemical principles. Physical methods include lithography, laser ablation and high-intensity radiation, whereas chemical methods comprise chemical reduction, electrochemical synthesis and photochemical reduction. 16,17 Comparisons between green synthesis and non-green synthesis may be made using life cycle assessment. There is no question that a non-green synthesis technique is a manufacturing process that consumes a significant amount of energy, with the contribution of electricity accounting for a substantial fraction of the total. <sup>18</sup> In addition, it will increase the environment's strain, particularly in the areas of greenhouse gas emissions and energy resources.<sup>19</sup> The current work aimed to synthesise Magnesium oxide nanoparticles (MgO NPs) using a non-thermal plasma technique and Anethum graveolens (dill) extract as a reducing and capping agent.

#### 2. METHODOLOGY

# 2.1 Preparation of Plant Extract

The dill plant has been cleaned with deionised water to eliminate dust and other impurities. Afterward, it is dried and ground. To prepare the dill extract, dissolve 10 g in 100 mL of deionised water, boil for 10 mins, and then filter using filter paper. Dill extract contains bioactive compounds such as polyphenols, flavonoids and terpenoids that act as reducing agents to reduce metal ions to NPs and as stabilising agents to prevent aggregation. A 1% concentration ensures the NPs are properly covered with the organic compounds present in the extract, thus decreasing aggregation and increasing stability.

The polyphenols and flavonoids in the dill extract are bioactive molecules that donate electrons to metal ions like Mg<sup>2+</sup>, reducing them to their zero-valent state and prompting NPs formation. The organic molecules in the dill extract bind to the NP's surface, forming a capping layer that prevents agglomeration. This stabilisation will maintain the NPs' nanoscale dimension and high surface area, which are essential for their antibacterial and catalytic properties.

The green synthesis of dill extract provides an eco-friendly alternative to chemical reducing agents like sodium borohydride and stabilisers like polyvinylpyrrolidone, making the synthesis process sustainable and biocompatible.

# 2.2 Synthesis of MgO NPs

Plasma-assisted reduction employs plasma, a partially ionised gas comprising ions, electrons and neutral species, to assist in the reduction of metal ions to NPs. Plasma offers energy and reactive species that augment the reduction reaction. The plasma produces reactive species (e.g., electrons, ions and radicals) that interact with the dill extract and metal ions, thereby promoting the reduction process. The synergy between plasma and dill extract improves the metal ions' reduction rate and the NPs' homogeneity and stability. Figure 1 illustrates the experimental schematic arrangement of a plasma jet apparatus. The direct current (DC) power source in this experiment was 12kV. The cathode was a hollow stainless steel tube. The anode was a Mg wire. 10 mL of dill extract was introduced into a pyrex beaker. The plasma projectile traversed the atmosphere at a gas flow rate of 3 (L/min). The plasma discharge nozzle was located approximately 2 cm above the surface of the deionised water. The discharge gas was argon with a purity of 99.99%. The metal was subjected to plasma treatment in the dill extract for 10 mins. The characteristics of the synthesised MgO NPs have been examined using various methodologies, such as X-ray diffraction (XRD), scanning electron microscope (SEM), energy dispersive X-ray spectroscopy (EDS) and ultraviolet-visible (UV-Vis).

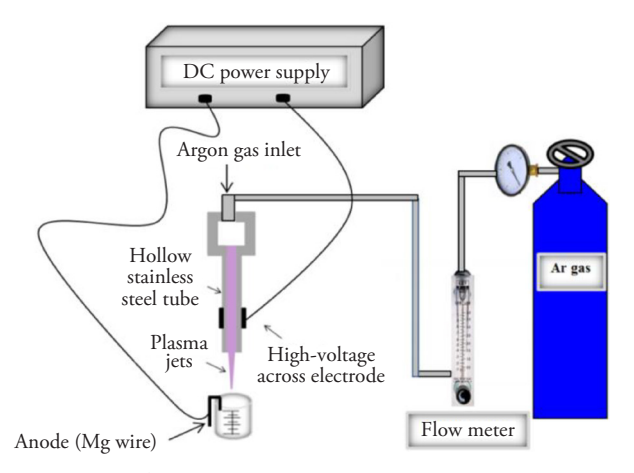


Figure 1: A diagram of the plasma jet apparatus used to synthesise MgO NPs.

## 2.3 Antibiofilm Activity Examine

MgO NPs have antimicrobial activity via many mechanisms, including generating reactive oxygen species (ROS), rupturing membranes, and releasing ions (Mg<sup>2+</sup>). The efficacy of antimicrobials is contingent upon cell wall composition and defensive mechanisms. Gram-negative bacteria may exhibit increased resistance owing to their outer barrier, which obstructs NPs penetration. Gram-positive bacteria, characterised by a more porous cell wall, would presumably exhibit increased susceptibility

to MgO NPs. The study sought to ascertain if MgO NPs exhibit a universal antibacterial effect or whether their activity varies depending on the kind of bacterium, namely gram-positive or gram-negative. The outcome may ascertain if the action method is constant, contingent upon the structural features of bacteria. Staphylococcus aureus (S. aureus), Klebsiella pneumonia (K. pneumonia) and Escherichia coli (E. Coli) bacterial species used in this study were provided by Mustansiriayah University Department of Biology. All tests were conducted in three independent repetitions, and the average findings were computed together with the standard deviation estimate (Mean ± SD). An experiment was conducted to evaluate the impact of MgO NPs on bacterial biofilm using a 96-well polystyrene flat-bottom plate with brain heart infusion (BHI) broth. To cultivate bacteria, BHI broth was heated to 37°C. After many days of culture dilution, the optical density (OD595) reached 0.137. Next, 80 μL of BHI broth with 2% sucrose and 20 μL of bacterial dilution were added to the wells of the microtiter plates. Also, after adding 100 µL of MgO NPs, the plates were kept at 37°C for 24 h. After being washed twice with phosphatebuffered saline to remove any leftover well fluids, the plates were left to dry at room temperature. Bacterial cells that were not bound were removed. A 200 µL crystal violet solution with 0.1% was used to stain the biofilm. Following the removal of the stain with 200 µL of pure ethanol, the optical density at 630 nm was detected using the ELISA reader. For the negative control, we used Luria-Bertani broth alone; for the positive controls, we used a bacterial solution that did not include MgO NPs to create a biofilm. There were three separate replications of the experiment. The formula below was used to find the MgO NPs induced inhibition rate.<sup>20,21</sup>

Inhibition biofilm rate (%) = 
$$\left(\frac{ControlOD - TreatedOD)}{ControlOD}\right) \times 100$$
 (1)

#### 3. RESULTS AND DISCUSSION

### 3.1 Physical Characterisations

#### 3.1.1 XRD analysis

XRD investigation utilised Cu-K $\alpha$  radiation within the 10°–80° (20) range. Figure 2 shows the XRD analysis of MgO NPs generated by dill extract with plasma reduction. The XRD peaks at 40.86° and 58.94° correspond to the (200) and (220) planes of cubic MgO NPs, respectively. The crystallographic parameters of the crystal phase corresponding to JCPDS card No. 89-7746.<sup>22</sup> A pronounced and powerful peak is evident in the XRD spectrum at (200), indicating the high crystallinity of MgO NPs. The average crystal size was measured by Debye-Scherrer formula (Equation 1), as reported in Table 1.<sup>23</sup>

$$D = \frac{k\lambda}{\beta \cos \cos \theta}$$
 (1)

Where  $\lambda$  denotes the wavelength of Cu-K $\alpha$  radiation,  $\beta$  represents the full-width half-maximum (FWHM) in radians, and  $\theta$  indicates the angle of diffraction (in radians). The determined average crystalline size for the synthesised MgO NPs was 38.93 nm.

The distinctive peaks of MgO manifest at particular positions contingent upon its crystal structure, typically a face-centred cubic (FCC) arrangement. The peaks of MgO are ascribed to reflections from planes such as (200) and (220), in accordance with Bragg's law (Equation 2):<sup>24</sup>

$$n\lambda = 2d\sin\sin\theta \tag{2}$$

Where,

 $\lambda$ : The wavelength of the X-rays.

*d* : The distance between the crystal planes.

 $\theta$ : The diffraction angle.

Furthermore, equations (3) and (4) were utilised to compute the dislocation density  $\delta$  and lattice strain  $\epsilon$ .<sup>25</sup>

$$\delta = \frac{n}{D^2} \tag{3}$$

$$\varepsilon = \frac{\beta \cos \cos \theta}{4} \tag{4}$$

The measured  $\delta$  and  $\epsilon$  values for the MgO NPs were  $8.49\times10^{-4}$  lines/m² and  $2.61\times10^{-3}$ , respectively. The values suggest that the nanomaterial exhibits commendable crystallinity with little crystalline flaws, as the defect density is low compared to materials with significant defects. The minimal defect density  $(8.49\times10^{-4}\ lines/m²)$  indicates a scarcity of slip lines (defects) within the crystal lattice. This signifies that the MgO NPs possess a somewhat uniform crystal structure, which is crucial for enhancing the mechanical and electrical properties of the material. A reduction in flaws results in constrained crystal boundaries, diminishing electronic dispersion or energy loss when the material is utilised in active systems like photocatalysis. In comparison, the crystal stress  $(2.61\times10^{-3})$  signifies a minor distortion in the crystal lattice. This stress arises from the nanoscale effect of the particles; wherein size reduction alters the lattice dimensions due to surface contact forces. The minimal crystal stress indicates that the surface effect of the NPs remains within acceptable limits,

not adversely impacting the material's functional performance. Rendering them appropriate for situations necessitating elevated stability and performance efficiency, including photocatalysis and water purification.

Supplementary peaks distinct from MgO may result from leftover organic components or salts in the dill extract that were not fully dissociated during preparation. Certain chemicals in the plant extract may interact with Mg during synthesis, producing new molecules (mixed oxides). The synthesised MgO may be polyphasic, creating additional phases of mixed oxides or distinct crystalline phases, denoted by (\*) in Figure 3.

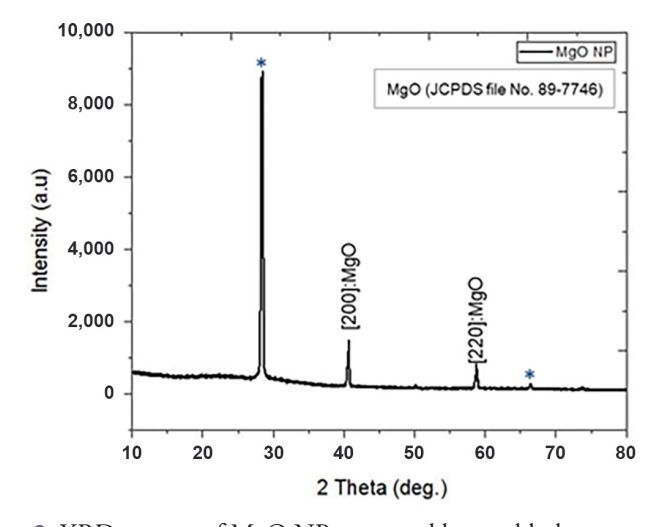


Figure 2: XRD pattern of MgO NPs prepared by a cold plasma method.

Table 1: Parameters calculation for XRD of MgO NPs.

Peak position (2θ°)	FWHM β (nm)	D (nm)	Average D (nm)
40.6801	0.319	27.74	38.93
58.7728	0.190	50.12	

*Note*: D = crystallite size

The crystalline structure of MgO NPs is crucial as it determines their reactivity and stability. Highly crystalline MgO NPs with diminutive crystallite sizes, as determined by XRD, have an increased surface area, hence augmenting their contact with microbial cells. The absence of any impure MgO phase guarantees that the observed antibacterial action is attributable only to MgO NPs, excluding the influence of other compounds. Reduced crystallite sizes may enhance the release of Mg<sup>2+</sup> ions, which are known to compromise microbial cell membranes and biofilm matrix.<sup>26</sup>

# 3.1.2 Field Emission Scanning Electron Microscopy analysis

The morphology observed in Field Emission Scanning Electron Microscopy (FE-SEM) images of MgO NPs displays dendritic patterns arising from the particles' growth and aggregation mechanisms during the manufacturing process. MgO NPs possess a cubic crystal structure, resulting in the anisotropic development of crystals in particular orientations. Dendritic branches form due to disparate growth rates at crystal surfaces, where the development velocity in some directions, such as crystallographic direction (200), exceeds that in others, such as (220). Dendritic growth may occur under specific conditions, such as rapid cooling or chemical barriers, such as plant extracts, rather than compact or spherical forms. The plasma jet technique generates a high-energy environment that results in the ionisation of material molecules and the creation of active plasma. The particles accumulate and crystallise upon rapid cooling of the active plasma, resulting in the observable branches. The plant extract serves as a growth-promoting agent, with chemical components like phenols inhibiting growth in some directions while encouraging branching. These structures offer an extensive surface area with an intricate three-dimensional configuration, rendering them unique. We note the presence of wide gaps between the branches. These spaces arise from the elevated evaporation rate or the repulsion among NPs during assembly. Furthermore, the dill extract comprises active chemical components, including phenols and terpenes, which function as reducing and stabilising agents. These compounds regulate the crystal growth rate and facilitate the creation of dendritic structures by minimising random agglomeration and promoting structural order. Figure 3 shows FE-SEM images for different scales.

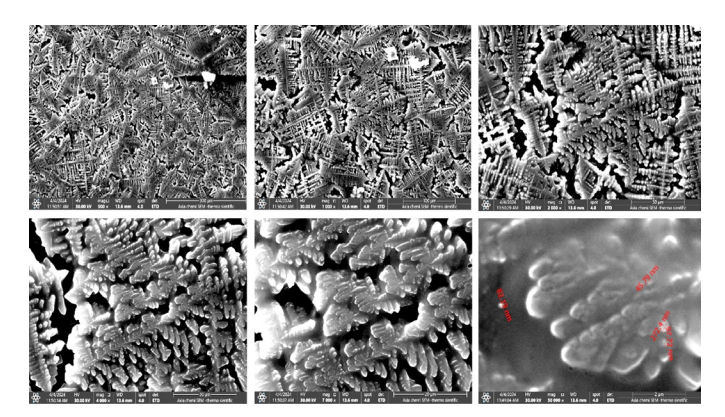


**Figure 3:** FE-SEM images of MgO NPs synthesised by plasma jet technique with dill extract plant at different scales.

The dimensions and architecture of NPs directly affect their penetration into biofilms and their interaction with microbial cells. Uniform and diminutive NPs (as verified by FE-SEM) exhibit superior penetration of biofilm EPS. The rough and uneven surface

shape, as shown by FE-SEM, enhances the adhesion of NPs to microbial cells, hence augmenting antibacterial efficacy. The efficacy of MgO NPs in disrupting biofilms is significantly influenced by their physical contact with the biofilm matrix, which is contingent upon their size and form.<sup>27</sup>

### 3.1.3 EDS analysis

By identifying X-rays emitted from the material when an electron beam bombards it, the EDS method determines the chemical composition of the studied region. The presence of peaks connected to the Mg and O elements in the MgO NPs was shown by the EDS spectra, which are displayed in Figure 5. The MgO NPs were pure based on the EDS analysis, which revealed no further impurity elements. Mg and oxygen (O) have corresponding weight percentages of 33% and 67%. The elemental mapping showed the MgO NPs' homogeneous distribution of Mg and O. According to the EDS spectra, which supported the verified XRD data, the plasma jet method successfully produced MgO NPs. Figure 4 illustrates the EDS analysis of MgO synthesised by green methods utilising dill; this spectrum illustrates the peaks of the elements in the sample according to the distinctive energy of each element. The prominent peak at Mg-K signifies Mg as a principal element, whereas the peak at O-K denotes the presence of O, a constituent of MgO. The uniform distribution of these elements signifies the sample's homogeneous synthesis of MgO. The signal intensity related to Mg and O corroborates the synthesis of MgO devoid of discernible contaminants.

The purity of MgO NPs, as verified by EDS, is crucial, since extraneous contaminants may impede antibacterial efficacy. The presence of Mg and O in the correct stoichiometric ratio guarantees the precise release of Mg<sup>2+</sup> ions, which disrupt microbial cell membranes and compromise the integrity of biofilms.<sup>28</sup>

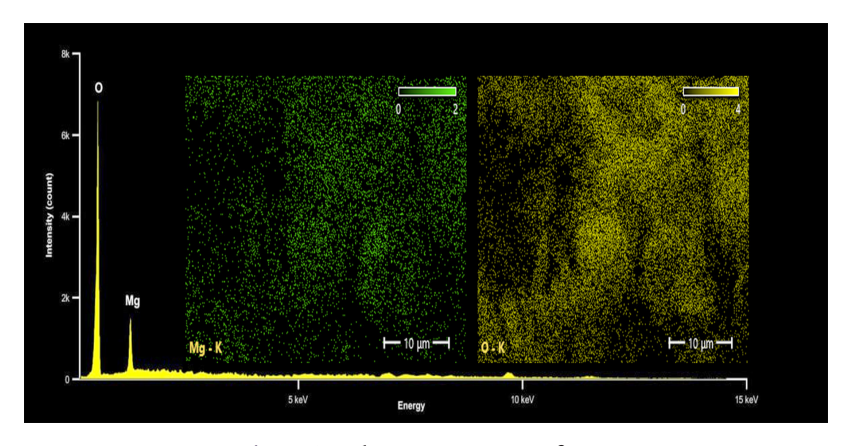


Figure 4: EDS and image mapping of MgO NPs.

### 3.1.4 UV-Vis analysis spectroscopy

The absorption spectrum of MgO NPs was measured using a UV-Vis spectrometer within the 200 nm-800 nm wavelength range. Figure 6 illustrates the UV-Vis spectrum, wherein the pronounced peak at 295 nm corroborates the synthesis of MgO NPs. The band gap energy of the synthesised MgO NPs was determined from the UV-Vis spectrum using the formula  $E_g = hv$ , where  $E_g$  represents the optical band gap energy, h denotes Planck's constant, and v signifies frequency. The estimated band gap energy of MgO NPs was observed to be 4.2 eV, in contrast to the bulk MgO, which exhibited a band gap energy of 7.8 eV. The reduced band gap energy is related to the existence of four-coordinated surface anions at the edges of MgO NPs, whereas the bulk materials contain six-coordinated surface anions. This observation aligns with the prior research conducted by Berger et al.<sup>30</sup> In addition to bulk materials, MgO with varying NPs sizes will also influence the band gap energy. Suresh documented a band gap of 5.6 eV for MgO NPs averaging 20 nm in size. The band gap of our MgO NPs, with an average particle size of around 28 nm (to be elaborated in the XRD section), is 4.2 eV, indicating that the band gap energy increases as particle size diminishes. In bulk solids, the energy levels are closely spaced, resulting in the formation of quasi-continuous bands. As one transitions to the nano regime, the spacing between energy levels increases, resulting in the observation of discrete energy levels.<sup>27</sup>

A significant optical characteristic is the bandgap. Consequently, the absorbance spectra can be employed to Tauc's direct transition Equation (5). To determine the MgO nanoparticles' absorption coefficients. The variables in the equation are delineated as follows:  $\alpha$  denotes the absorption coefficient, h signifies Planck's constant,  $\nu$  indicates the frequency of the incident photon, A is a constant (A = 0.9),  $E_g$  represents the optical energy gap, and r is a variable dependent on the type of transition. For a permitted direct transfer, r equals 2. A prevalent technique for determining the bandgap involves plotting photon energy ( $h\vartheta$ ) versus ( $\alpha$ hv) $^r$  and extrapolating the linear portion to the axis intercept, as illustrated in Figure 5.

$$(\alpha h \vartheta)^r = A(h \vartheta - E_g) \tag{5}$$

A typical method for finding the optical band gap energy of NPs is to plot the experimental absorbance data. The bandgap energy was directly measured from  $\lambda$  cut using Planck's rule, as indicated in Equation (6).<sup>23</sup>

$$E_{g} = \frac{hc}{\lambda} \tag{6}$$

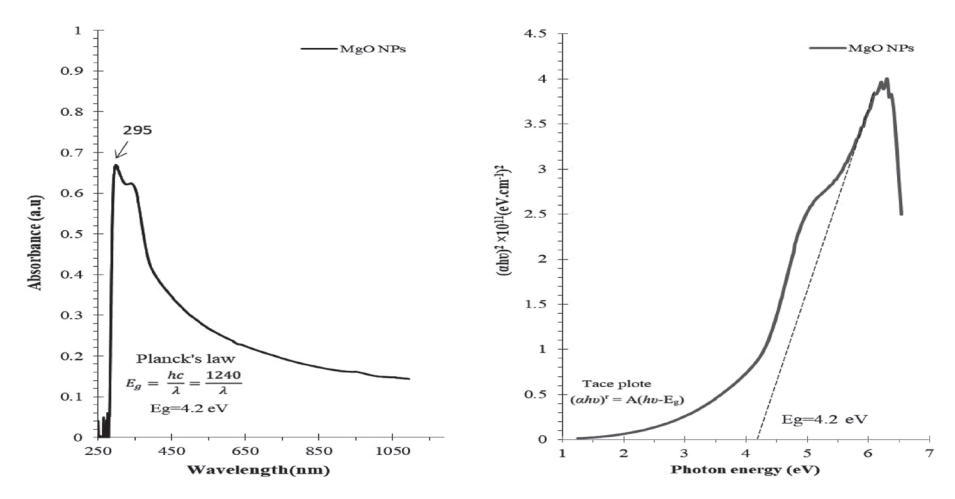


Figure 5: UV-Vis analysis of MgO NPs prepared cold plasma.

The energy band gap, determined using UV-Vis measurements, regulates the formation of ROS in MgO NPs. A low energy band gap facilitates increased ROS formation, which is essential for antibacterial and antibiofilm efficacy. ROS decomposes microbial cell membrane constituents, proteins and DNA, resulting in microbial eradication and biofilm degradation.<sup>29</sup>

# 3.2 Antibiofilm Activity of MgO NPs

They adhere to surfaces, increasing the complex's resistance to external antibacterial measures. The biofilm matrix is composed of proteins, fibrin and polysaccharides. UV radiation, temperature fluctuations, biocides, desiccation and humoral and cellular immune responses are detrimental physical, biological and chemical environmental variables against which biofilms protect themselves. Bacterial biofilms are difficult to eradicate with the same amount of antibiotics as free-floating or isolated bacteria. The development of antibiotic resistance in biofilms facilitates the ongoing spread of infections. Biofilm formation is associated with increased antibiotic resistance in several types of bacteria, which is necessary for therapeutic purposes. Consequently, developing novel antibacterial agents that can effectively target biofilms is essential. This research evaluated the antibiofilm efficacy of MgO NPs against three bacterial strains:

*E. coli*, *S. aureus* and *K. pneumoniae*. Figure 6 illustrates that *K. pneumoniae*, *E. coli* and *S. aureus* treated with MgO NPs significantly reduced biofilm development. Treatment with 10 mgL<sup>-1</sup> of MgO NPs resulted in the highest % inhibition against *S. aureus*, 42.74%, followed by *E. coli*, 34.94% and *K. pneumoniae*, 33.82%, as listed in Table 2. Figure 6 illustrates that *K. pneumoniae*, *E. coli* and *S. aureus* biofilm development was suppressed upon treatment with MgO NPs.

1 0											
Bacterial type	Befo	Before treatment (Control)			After treatment						
	1st OD	2 <sup>nd</sup> OD	3 <sup>rd</sup> OD	Mean	1st OD	2 <sup>nd</sup> OD	3 <sup>rd</sup> OD	Mean	Inhibition rate (% ± S.D)		
K. pneumoniae	0.673	0.683	0.616	0.657	0.405	0.470	0.432	0.434	33.82 ± 5.41		
E. coli	0.673	0.632	0.687	0.664	0.468	0.451	0.377	0.432	$34.94 \pm 9.04$		
S. aureus	0.647	0.611	0.644	0.634	0.383	0.387	0.319	0.363	$42.74 \pm 7.08$		

Table 2: Inhibition biofilm of Staphylococcus aureus, Klebsiella pneumoniae, and Escherichia coli strains as well as the impact of MgO NPs.

Note: OD = optical density

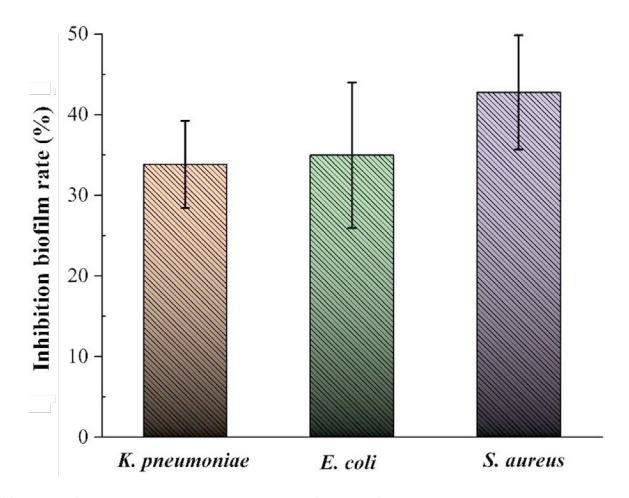


Figure 6: Effects of MgO NPs against biofilm of S. aureus, K. pneumoniae and E. coli.

Research conducted in the past has shown a correlation between smaller particle sizes and higher toxicity levels. It has been conclusively demonstrated that the size of NPs significantly influences the antibacterial activity. Smaller NPs often exhibit enhanced surface area-to-volume ratios compared to their bigger counterparts, enhancing their efficacy in interacting with microbial cell walls. The increased contact enhances antibacterial effectiveness. This is achieved by allowing an increased generation of ROS, enhanced infiltration into microbial cells and more efficient disruption of cell membranes. The nanoscale size of MgO particles, validated by XRD, is anticipated to improve their antibacterial effectiveness via the above methods,<sup>31,32</sup> Indirect interactions also involve the production of ROS and metal ions, which may occur either within or outside the cell.<sup>33</sup> Interactions between NPs and bacterial systems can potentially cause cellular absorption, ROS formation and metal ion release, among other things. The generation of ROS is a key mechanism by which NPs cause damage to bacterial cells.<sup>34</sup>

The researchers found that at a concentration of 40 mM, Mg<sup>2+</sup> could kill stationaryphase S. aureus cells and disrupt the membranes of model S. aureus, indicating that the ions were active on the cell membrane. In contrast to S. aureus, E. coli and Bacillus subtilis (B. subtilis) exhibit no change in survival after being subjected to equivalent treatment with these two cations, which suggests that these cations might have a species specific effect on S. aureus.35 According to all of these data, Mg2+ may have a role in the purposeful eradication of S. aureus infections, especially those that are resistant to antibiotics, which leads to the likelihood that Mg<sup>2+</sup> may play a function in elimination. Gram-negative bacteria's cell walls are mostly composed of peptidoglycan, lipopolysaccharide and lipids, suggesting their unique structure may also play a role in this occurrence. On the other hand, gram-positive bacteria and other microbes have large peptidoglycan structures in their cell walls.<sup>36–38</sup> MgO is an insoluble non-volatile oxide with high redox potential resulting from the firm ionic bond between Mg<sup>2+</sup> and O<sup>2-</sup>. Redox activity of MgO NPs is mainly due to the formation of ROS, e.g., superoxide radicals (O<sub>2</sub>), hydroxyl radicals (OH•) and hydrogen peroxide (H<sub>2</sub>O<sub>2</sub>) on irradiation or in water. With exposure to light irradiation (such as UV light), electrons from the valence band of MgO can be excited into the conduction band, generating holes. Electrons and holes may interact with oxygen and water to produce ROS.<sup>39-41</sup>

### 4. CONCLUSIONS

This study successfully synthesised MgO NPs via a green plasma-assisted reduction method using dill extract as a stabilising agent. This eco-friendly approach proved to be simple, non-toxic, rapid and effective for NPs production. XRD analysis confirmed that the synthesised MgO NPs possess a cubic polycrystalline structure, with an average crystallite size of approximately 38.93 nm. FE-SEM images revealed a distinctive dendritic morphology of the NPs, while UV-Vis spectroscopy indicated an absorption peak at 295 nm, corresponding to a band gap energy of 4.2 eV. Biological evaluation demonstrated that the green-synthesised MgO NPs exhibited significant antibiofilm activity, particularly against S. aureus, with moderate effects against K. pneumoniae and E. coli. These findings suggest that MgO NPs hold promising potential for biomedical applications, especially in combating biofilm-associated infections. However, further investigations, including cytotoxicity assessments and evaluations under different concentrations and conditions, are required to establish their safety and effectiveness fully. Additionally, optimisation of the synthesis parameters is crucial to achieve better control over particle size, shape and stability, facilitating their future scalability and commercialisation in various sectors.

#### 5. ACKNOWLEDGEMENTS

This study is supported by the Department of Biology, College of Science, Mustansiriayah University.

#### 6. REFERENCES

- 1. Nima, G. et al. (2021). Antibacterial efficacy of non-thermal atmospheric plasma against *Streptococcus mutans* biofilm grown on the surfaces of restorative resin composites. *Sci. Rep.*, 11(1), 23800. https://doi.org/10.1038/s41598-021-03192-0
- 2. Francolini, I. & Donelli, G. (2010). Prevention and control of biofilm-based medical-device-related infections. *FEMS Immunol. Med. Microbiol.*, 59(3), 227–238. https://doi.org/10.1111/j.1574-695X.2010.00665.x
- 3. Dongari-Bagtzoglou, A. (2008). Mucosal biofilms: Challenges and future directions. Expert Rev. Anti. Infect. Ther., 6(2), 141–144. https://doi.org/10.1586/14787210 .6.2.141
- 4. Alkawareek, M. Y. et al. (2012). Eradication of *Pseudomonas aeruginosa* biofilms by atmospheric pressure non-thermal plasma. *PLOS One*, 7(8), 0044289. https://doi.org/10.1371/journal.pone.0044289
- 5. Hall-Stoodley, L. et al. (2004). Bacterial biofilms: From the natural environment to infectious diseases. *Nat. Rev. Microbiol.*, 2(2), 95–108. https://doi.org/10.1038/nrmicro821
- 6. Donlan, R. M. & Costerton, J. W. (2002). Biofilms: Survival mechanisms of clinically relevant microorganisms. *Clinic. Microbiol. Rev.*, 15(2), 167–193. https://doi.org/10.1128/cmr.15.2.167-193.2002
- 7. Pandit, S. et al. (2015). Effect of 1-minute fluoride treatment on potential virulence and viability of a cariogenic biofilm. *Caries Res.*, 49(4), 449–457. https://doi.org/10.1159/000434731
- 8. Singh, P. et al. (2020). A sustainable approach for the green synthesis of silver nanoparticles from Solibacillus isronensis sp. and their application in biofilm inhibition. *Molecules*, 25(12), 2783. https://doi.org/10.3390/molecules25122783
- 9. Rodríguez-Hernández, A. P. et al. (2023). Antibacterial properties in vitro of magnesium oxide nanoparticles for dental applications. *Nanomater.*, 13(3), 502. https://doi.org/10.3390/nano13030502
- 10. Raghunath, A. & Perumal, E. (2017). Metal oxide nanoparticles as antimicrobial agents: A promise for the future. *Int. J. Antimicrob. Agents*, 49(2), 137–152. https://doi.org/10.1016/j.ijantimicag.2016.11.011
- 11. Mazhir, S. N. et al. (2018). The effect of gas flow on plasma parameters induced by microwave. *Baghdad Sci. J.*, 15(2), 0205–0205. https://doi.org/10.21123/bsj.2018 .15.2.0205
- 12. Mohammed, R. S. et al. (2024). Synthesize of ZnO and CuO nanoparticles with plasma jet at different treatment times and testing its optical parameters with UV-Vis-NIR. *Appl. Phys. A*, 130(8), 533. https://doi.org/10.1007/s00339-024-07651-z

- 13. Surya, M. et al. (2025). One pot Hypnea valentiae mediated synthesis of silver doped curcumin nanoparticles and their evaluation of antibacterial, anti-inflammatory and anticancer activity. *J. Ind. Eng. Chem.*, 149, 374–385. https://doi.org/10.1016/j.jiec.2025.01.051
- Mohammed, R. S. et al. (2023). Histological, haematological, and thyroid hormones toxicity of female rats orally exposed to CuO/ZnO core/shell nanoparticles synthesized by Ar plasma jets. *Arch. Toxicol.*, 97(4), 1017–1031. https://doi.org/10.1007/s00204-023-03462-y
- 15. Mohammed, S. R. & Ali, A. H. (2025). Using laser ablation to prepare nano nickel and studying optical properties. *J. Opt.*, 1–9. https://doi.org/10.1007/s12596-025-02477-1
- Vairamuthu, S. et al. (2024). Clove mediated synthesis of Ag-ZnO doped fucoidan nanocomposites and their evaluation of antibacterial, antioxidant and cytotoxicity efficacy study. *Res. Chem.*, 11, 101783. https://doi.org/10.1016/j.rechem.2024.101783
- 17. Mazhir, S. N., Aadim, K. A., Al-Halbosiy, M. M., & Abdalameer, N. K. (2021). Cytotoxic activity of green zinc selenide nanoparticles against Hep-G2 cell lines. *Indian J. Forensic Med. Toxicol.*, 15(1), 2072–2078.
- 18. Shanan, Z. J. et al. (2022). Green method of CuO NPs by using Eucalyptus camaldulensis aqueous extract with cold plasma, and its effect on biofilm formation. *Int. J. Nanosci.*, 21(03), 2250020. https://doi.org/10.1142/S0219581X2250020X
- 19. Noori, A. S. et al. (2024). Pulsed Nd: YAG laser-assisted synthesis of aluminum oxide nanoparticles with clove extract: Evaluating their antibacterial activity against mutant strain of streptococcus mutans. *Plasmonics*, 1–11. https://doi.org/10.1007/s11468 -024-02626-5
- 20. Ahmed, R. S. et al. (2024). Biological activity of MgO nanoparticle synthesis by plasma-assisted reduction method. *Phys. Scr.*, 99(11), 115901. https://doi.org/10.1088/1402-4896/ad7dbc
- 21. Nouri, A. et al. (2018). Diffusion of Cu Ions into Nanoclay by Molten Salt Ion Exchange for Antibacterial Application. *J. Phys. Sci.*, 29(1), 31–42. https://doi.org/10.21315/jps2018.29.1.3
- 22. Somanathan, T. et al. (2016). MgO nanoparticles for effective uptake and release of doxorubicin drug: pH sensitive controlled drug release. *J. Nanosci. Nanotechnol.*, 16(9), 9421–9431. Doi: https://doi.org/10.1166/jnn.2016.12164
- 23. Abbas, B. H. et al. (2024). Synthesis of copper oxide nanostructures by Ar plasma jet and study of their structural and optical properties. *Iraqi J. Sci.*, 65(4), 1999–2006. https://doi.org/10.24996/ijs.2024.65.4.18
- 24. Murbat, H. H. et al. (2018). Effects of non-thermal argon plasma produced at atmospheric pressure on the optical properties of CdO thin films. *Baghdad Sci. J.*, 15(2), 0221–0221. https://doi.org/10.21123/bsj.2018.15.2.0221
- 25. Muhaymin, A. et al. (2024). Green synthesis of magnesium oxide nanoparticles using *Hyphaene thebaica* extract and their photocatalytic activities. *Sci. Rep.*, 14(1), 20135. https://doi.org/10.1038/s41598-024-71149-0
- 26. Niknam, Z. et al. (2020). Osteogenic differentiation potential of adipose-derived mesenchymal stem cells cultured on magnesium oxide/polycaprolactone nanofibrous scaffolds for improving bone tissue reconstruction. *Adv. Pharma. Bullet.*, 12(1), 142. https://doi.org/10.34172/apb.2022.015

- 27. Hajipour, M. J. et al. (2012). Antibacterial properties of nanoparticles. *Trends Biotechnol.*, 30(10), 499–511. https://doi.org/10.1016/j.tibtech.2012.06.004
- 28. Slomberg, D. L. & Schoenfisch, M. H. (2012). Silica nanoparticle phytotoxicity to Arabidopsis *thaliana*. *Environ. Sci. Technol.*, 46(18), 10247–10254. https://doi.org/10.1021/es300949f
- 29. Raghupathi, K. R. et al. (2011). Size-dependent bacterial growth inhibition and mechanism of antibacterial activity of zinc oxide nanoparticles. *Langmuir*, 27(7), 4020–4028. https://doi.org/10.1021/la104825u
- 30. Berger, T. et al. (2005). Trapping of photogenerated charges in oxide nanoparticles. *Mater. Sci. Eng. C*, 25(5–8), 664–668. https://doi.org/10.1016/j.msec.2005.06.013
- 31. Suresh, S. (2014). Investigations on synthesis, structural and electrical properties of MgO nanoparticles by sol–gel method. *J. Ovonic. Res.*, 10(6), 205–210.
- 32. Shanan, Z. J. et al. (2022). Zinc oxide nanoparticle properties and antimicrobial activity. *Int. J. Nanosci.*, 21(03), 2250017. https://doi.org/10.1142/S0219581X225 0017X
- 33. Naif, H. A. et al. (2022). Spectral behaviour of the low concentrations of Coumarin 334 with broadband cavity enhanced absorption spectroscopy. *Baghdad Sci. J.*, 19(2), 0438–0438. https://doi.org/10.21123/bsj.2022.19.2.0438
- 34. Falih, M. S. et al. (2024). Synthesis and characterization of new Azo Dye Derived from Sulfamethaxolevia Diazonium Reaction and Study its Abilityas an Acid-base Indicator. *Al-Mustansiriyah J. Sci.*, 35(2), 1–8. https://doi.org/10.23851/mjs.v35i2.1375
- 35. Mohammed, R. S. & Al-Marjani, M. F. (2024). DBD plasma as a practical approach to sterilization of dental instruments. *Phys. Scr.*, 99(4), 045601. https://doi.org/10.1088/1402-4896/ad2e5a
- 36. Abdulrahman, A. T. et al. (2022). Detection of Helicobacter Pylori's virulence gene (UreA) and its influence on the result of rapid urease test (RUT). *Al-Mustansiriyah J. Sci.*, 33(4), 42–48. https://doi.org/10.23851/mjs.v33i4.1152
- 37. Mazhir, S. N. et al. (2022). Bio-synthesis of (Zn/Se) core-shell nanoparticles by micro plasma-jet technique. *Int. J. Nanosci.*, 21(05), 2250041. https://doi.org/10.1142/S0219581X22500417
- 38. Pourabolghasem, H. et al. (2016). Antibacterial activity of copper-doped montmorillonite nanocomposites prepared by alkaline ion exchange method. *J. Phys. Sci.*, 27(2). http://dx.doi.org/10.21315/jps2016.27.2.1
- 39. Masbah, M. S. et al. (2024). Microwave crosslinked chitosan/green fluorescent carbon nanoparticles film: Comprehensive characterisation and antimicrobial performance. *J. Phys. Sci.*, 35(2), 47–65. https://doi.org/10.21315/jps2024.35.2.4
- 40. Flemming, H. C. et al. (2016). Biofilms: An emergent form of bacterial life. *Nature Rev. Microbiol.*, 14(9), 563–575. https://doi.org/10.1038/nrmicro.2016.94
- 41. Talib, W. R. et al. (2024). Potential biological and optoelectronic applications of AgO: ZnO nanocomposite synthesized by green approach. *Eur. Phys. J. Plus*, 139(12), 1118. https://doi.org/10.1140/epjp/s13360-024-05920-7